The Astrophysical Journal, 988:275 (9pp), 2025 August 1 https://doi.org/10.3847/1538-4357/ade87b

Magellanic Accretion-powered Pulsars Studied via an Unscented Kalman Filter

Dimitris M. Christodoulou[1], Joseph O'Leary[2], Andrew Melatos[2], Tom Kimpson[2], Sayantan Bhattacharya[1], Nicholas J. O'Neill[2], Silas G. T. Laycock[1], and Demosthenes Kazanas[3]

[1] Lowell Center for Space Science and Technology, University of Massachusetts Lowell, Lowell, MA 01854, USA; dimitris_christodoulou@uml.edu
[2] School of Physics and OzGrav, University of Melbourne, Parkville, VIC 3010, Australia; joe.oleary@unimelb.edu.au, amelatos@unimelb.edu.au
[3] NASA/GSFC, Astrophysics Science Division, Code 663, Greenbelt, MD 20771, USA

Received 2025 March 28; revised 2025 June 20; accepted 2025 June 24; published 2025 July 30

Abstract

Magnetized high-mass X-ray binary pulsars accreting from a surrounding disk have been recently studied by a time-dependent Kalman filter (KF) model of accretion capable of studying correlations between dynamical variables and producing time series of their behaviors. We return to the intrinsic KF equations that describe the accretion process, and we rewrite them in simpler forms that allow for straightforward interpretations and a deeper understanding of the KF output data. We describe the influence of the KF defined frequencies β_1, β_2, and γ_Ω, and we investigate the surface dipolar magnetic fields of 24 Magellanic pulsars produced by the KF analysis in comparison to the values obtained from standard accretion theory using the long-term trending changes of the pulsar spin periods (known as the long-term P-dot values). Good agreement is obtained over a wide range of pulsar spin periods when the KF magnetic field values are scaled down to the propeller regime by a factor of $\sqrt{1 - \omega_s}$, where $\omega_s = \beta_2/\beta_1$ is the fastness parameter that also distinguishes the regime of "stable polar" accretion ($\omega_s > 0.6$) from Rayleigh–Taylor-driven "two-tongue equatorial" ($\omega_s < 0.45$) matter inflow.

Unified Astronomy Thesaurus concepts: High mass x-ray binary stars (733); Astronomical instrumentation (799); Magnetic fields (994); Pulsars (1306)

1. Introduction

1.1. Magellanic High-mass X-Ray Binaries

The Small Magellanic Cloud (SMC), a dwarf irregular satellite galaxy of the Milky Way, hosts more than 120 known high-mass X-ray binaries (HMXBs; F. Haberl et al. 2022). The optical counterparts in such systems, with masses comparable to or exceeding 10 $M_\odot$, are commonly Be stars, with the notable exception of SMC X-1, whose optical counterpart is a B0 Ib supergiant donor star (F. Haberl & R. Sturm 2016). One ascribes the large population of HMXBs in the SMC to recent star formation activity (J. Galache et al. 2008), low metal content (V. Antoniou et al. 2010), and significant tidal interactions with the nearby Large Magellanic Cloud (L. T. Gardiner & M. Noguchi 1996).

Coherent X-ray timing observations from long-term timing campaigns with the Rossi X-ray Timing Explorer (RXTE; K. Jahoda et al. 2006), XMM-Newton (L. Strüder et al. 2001), and Chandra (G. P. Garmire et al. 2003) space-based observatories have been instrumental in estimating the stellar and orbital properties of SMC HMXBs (J. Galache et al. 2008; L. Townsend et al. 2011; H. Klus et al. 2014; M. Coe et al. 2015; D. M. Christodoulou et al. 2016, 2017; J. Yang et al. 2017).

In an essential project, J. Yang (2017) and J. Yang et al. (2017) developed an analysis pipeline to process 37,779 RXTE, XMM-Newton, and Chandra archival X-ray timing observations of 65 accretion-powered pulsars in the SMC, yielding pulse period $P(t)$ and aperiodic X-ray luminosity $L(t)$ time series for 53 SMC HMXBs between years 1997 and 2014. The foregoing time series contain important time-dependent information about the complex physics that takes place at the disk−magnetosphere boundary of such accretion-powered pulsars.

1.2. Measuring the Magnetic Field Strengths of HMXBs

Cyclotron lines observed in the X-ray spectra of accretion-powered pulsars yield direct measurements of the surface magnetic field strengths $B_\star$ (P. A. Becker et al. 2012; O. Nishimura 2013, 2014, 2015; A. A. Mushtukov et al. 2015, 2021; D. M. Christodoulou et al. 2019; R. Staubert et al. 2019). Although important diagnostic tools for accretion-powered pulsars, cyclotron lines have been observed in only two SMC HMXB systems, namely SMC X-2 (G. K. Jaisawal & S. Naik 2016) and SXP 15.3 (C. Maitra et al. 2018). Accordingly, researchers commonly resort to inferring stellar properties, such as the surface magnetic field strength $B_\star$ and the magnetic dipole moment μ of accretion-powered pulsars, using time-averaged pulse period $\langle P(t)\rangle$ and luminosity $\langle L(t)\rangle$ observations (W. C. G. Ho et al. 2014; H. Klus et al. 2014; D. Mukherjee et al. 2015), coupled with phenomenological accretion torque models, such as the canonical magnetocentrifugal paradigm (P. Ghosh & F. Lamb 1979) and the hyperbolic tangent propeller transition and trapped disk models (C. R. D'Angelo & H. C. Spruit 2010, 2012; C. R. D'Angelo 2017), among others (J. J. R. Stierhof et al. 2025). Important time-dependent information, e.g., temporal (anti)correlations, is lost when employing the $\langle P(t)\rangle$ and $\langle L(t)\rangle$ time-averaged observables.

Recently, it has been shown that, by using a linear Kalman filter (KF), one can track the stochastic fluctuations occurring in pulse period $P(t)$ and X-ray luminosity $L(t)$ time series of HMXBs near spin equilibrium (A. Melatos et al. 2023; J. O'Leary et al. 2024b). This new framework yields time-resolved estimates of three hidden state variables, namely the mass accretion rate, the Maxwell stress at the disk–magnetosphere boundary, and the radiative efficiency of the accretion process, as well as the angular velocity of the star. The framework was extended to disequilibrium situations, yielding thus new estimates of the magnetic moments and time-resolved estimates of the mass accretion rates and the Maxwell stresses, shedding light on self-healing Rayleigh–Taylor (RT) hydromagnetic instabilities at the disk–magnetosphere boundary for a sample of 24 SMC HMXBs. This analysis has made use of an unscented KF (J. O'Leary et al. 2024a, 2025).

1.3. The Unscented Kalman Filter Approach

The unscented (nonlinear) KF model of disk accretion onto a compact object follows and analyzes in detail the temporal fluctuations of the observed physical quantities, producing thus sets of intrinsic time-dependent variables along with their ensemble averages. The model has been recently applied by J. O'Leary et al. (2024a, 2025) to 24 HMXB pulsars observed by RXTE in the SMC over a period of ~20 yr (H. Klus et al. 2014; D. M. Christodoulou et al. 2016, 2017, 2018a; C. R. D'Angelo 2017; J. Yang et al. 2017, and references therein).

Application of the unscented KF model to an astrophysics problem is new, and the equations have taken some forms previously not featured in related research. In this work, we revisit the formulations of the KF accretion model (A. Melatos et al. 2023; J. O'Leary et al. 2024b, 2024a), we rewrite the adopted equations in simpler forms, and we discuss the physics behind them. Our main goals are to analyze the KF-defined intrinsic frequencies (β_1, β_2, γ_Ω) and to investigate the discrepancies in the estimates of pulsar magnetic fields between the KF model and other previous models (H. Klus et al. 2014; H. Klus 2015; D. M. Christodoulou et al. 2017; C. R. D'Angelo 2017).

1.4. Outline

In Section 2, we describe and analyze the equations of accretion implemented in the unscented KF model.

In Section 3, we compare and discuss the various estimates of the magnetic fields obtained by different methods for the 24 HMXB pulsars of the J. O'Leary et al. (2024a, 2025) sample (the "SMC-24" sample).

In Section 3.3, we conclude with a best fit of the averaged values of the magnetic fields obtained from two methods (KF and spin period derivative or "P-dot") versus pulsar spin period.

2. Equations of Kalman Filter Accretion and Their Physical Interpretations

It is common practice to write the equations of accretion in complicated forms involving rational powers of various implicitly interrelated quantities, and the particular accretion model incorporated into the unscented KF is no exception. Such complicated equations are commonly justified, as they provide computational efficiency, but they are hard to interpret physically, which leaves us with typically interpreting the vast numerical output produced by the computations.

Here we recast the fundamental equations of the KF model in their simplest possible forms that allow for straightforward interpretations. In the reductions below, fluctuating variables are represented by their "mean" (ensemble-averaged) values, and stellar quantities are marked by star symbols.

2.1. Kalman Filter Accretion Equations

Two slightly different sets of computational equations implemented in the unscented KF model can be found in A. Melatos et al. (2023) and J. O'Leary et al. (2024b, 2024a, 2025). The equations of the KF disk accretion that we have transformed to simpler forms come from the latter works,[4] and they are summarized below.

The KF torque exerted onto the pulsar is described by the phenomenological equation

$$I_\star \frac{d\Omega_\star}{dt} = (1 - \omega_s) Q \sqrt{G M_\star R_m} \,. \tag{1}$$

Here $I_\star$ is the moment of inertia of a pulsar of mass $M_\star$ spinning with angular velocity $\Omega_\star$, t denotes time, ω_s is the so-called fastness parameter (P. Ghosh & F. Lamb 1979; Y.-M. Wang 1995), Q is the mass inflow rate (widely known as "M-dot"), G is the Newtonian gravitational constant, and R_m is the magnetospheric radius.

The magnetospheric radius is given by

$$R_m = (2\pi^{2/5})^{-1} (G M_\star)^{1/5} \left(\frac{Q}{S}\right)^{2/5} , \tag{2}$$

and, as usual, the corotation radius is given by

$$R_c = (G M_\star)^{1/3} \Omega_\star^{-2/3} \,. \tag{3}$$

In spin equilibrium (W. C. G. Ho et al. 2014), the (positive) mass inflow rate is given by

$$Q = \frac{I_\star \Omega_\star^{4/3} \gamma_\Omega}{(G M_\star)^{2/3}} = \frac{I_\star \gamma_\Omega}{R_c^2} , \tag{4}$$

and the Maxwell stress (J. D. Jackson 1962) that balances the ram pressure at the inner edge of the disk is given by

$$S = \frac{I_\star \Omega_\star^3 \gamma_\Omega}{2^{5/2} \pi G M_\star} = \frac{1}{4\pi\sqrt{2}} \left(\frac{\mathcal{L}_\star \gamma_\Omega}{R_c^3}\right) . \tag{5}$$

Here γ_Ω is the quotient of the maximum torque on the pulsar (Equation (14) below) to its angular momentum $\mathcal{L}_\star = I_\star \Omega_\star$; thus, $\gamma_\Omega = d(\ln \mathcal{L}_\star)/dt$ is a frequency with dimensions of $[\mathrm{time}]^{-1}$.

The frequencies β_1, β_2 returned by the nonlinear version of the KF are given in Section 2.4 of J. O'Leary et al. (2024a), viz.,

$$\beta_1 = \frac{(G M_\star)^{3/5}}{(2\pi^{2/5})^{1/2} I_\star \Omega_\star} \left(\frac{Q^6}{S}\right)^{1/5} , \tag{6}$$

and

$$\beta_2 = \frac{(G M_\star)^{2/5}}{(2\pi^{2/5})^2 I_\star} \left(\frac{Q^9}{S^4}\right)^{1/5} . \tag{7}$$

---

[4] In J. O'Leary et al. (2024a, 2024b, 2025), the freefall speed V_{ff} and the Maxwell stress S are defined each with an additional factor of 2, as, e.g., in J. Frank et al. (2002) and K. Menou et al. (1999), respectively. Details are given in part (4) of Section 2.2 below.

Table 1
Ensemble-averaged Length Scales and Their Ratios Produced by the KF Model for the SMC-24 Sample of Magellanic HMXB Pulsars

No.	SXP Name	$P_\star$ (s)	R_c (Mm)	R_m (Mm)	ω_s	ℓ
1	4.78[a]	4.780	4.76	4.46	0.914	21.12
2	6.85[a]	6.851	6.05	5.98	0.964	24.46
3	8.88	8.901	7.20	2.77	0.238	16.64
4	11.5[a]	11.475	8.53	8.47	0.981	29.10
5	11.9[a]	11.866	8.72	8.65	0.990	29.41
6	18.3[a]	18.371	11.67	9.62	0.738	31.02
7	51.0	51.024	23.05	8.00	0.206	28.28
8	59.0	58.866	25.36	9.83	0.233	31.35
9	82.4	82.432	31.74	11.95	0.231	34.57
10	95.2	95.218	34.94	12.12	0.207	34.81
11	101	101.357	36.43	14.91	0.259	38.61
12	138[a]	138.001	44.75	39.02	0.815	62.46
13	152[a]	152.022	47.74	42.72	0.843	65.36
14	172	171.926	51.82	20.16	0.246	44.90
15	202A	201.558	57.61	32.77	0.253	57.25
16	214	214.121	59.98	24.54	0.258	49.54
17	264[a]	263.602	68.90	59.76	0.804	77.31
18	292[a]	291.974	73.76	70.30	0.919	83.84
19	293[a]	292.971	73.92	53.80	0.619	73.35
20	323	318.859	78.22	32.16	0.253	56.71
21	523	523.049	108.79	45.63	0.256	67.55
22	565	565.070	114.54	44.91	0.248	67.02
23	756	751.105	138.47	58.11	0.256	76.23
24	893	893.139	155.42	63.98	0.257	79.99

Note. Here the magnetospheric ratios are $\omega_s = (R_m/R_c)^{3/2}$ and $\ell = \sqrt{R_m/R_\star}$, where $R_\star = 10$ km.

[a] Pulsar near spin equilibrium.

Finally, the surface dipolar magnetic moment of the pulsar is determined by

$$\mu_\star = (GM_\star Q^2/8)^{3/5}\,(2\pi S)^{-7/10}\,. \tag{8}$$

A reduced form of this equation, valid in spin equilibrium, viz.,

$$(\mu_\star)_{\rm se} = 2^{-3/4}\,(GM_\star)^{5/6}\,\Omega_\star^{-7/6}\,Q^{1/2}\,, \tag{9}$$

is obtained for $\omega_s = 1$ from Equation (22) specified in part (6) of Section 2.2, and it is used in part (8) of Section 2.2.

2.2. Standard Accretion Equations

(1) *Length scales and angular momentum transfer rates.* From the three fundamental length scales of the model (R_m, R_c, and $R_\star$), we define two comparative ratios, viz.,

$$R_m/R_c \;\equiv\; \omega_s^{2/3} \tag{10}$$

and

$$R_m/R_\star \;\equiv\; \ell^2\,, \tag{11}$$

where ω_s is the fastness parameter and ℓ is the ratio of angular momentum transfer rates related to the disk's mass inflow rate $Q > 0$ and the pulsar's spin change $I_\star|d\Omega_\star/dt|$ during accretion events with $\omega_s \ll 1$ (D. M. Christodoulou et al. 2018a), viz.,

$$\ell = \frac{I_\star|d\Omega_\star/dt|}{Q\,R_\star V_{\rm K\star}} \equiv \frac{d\mathcal{L}_\star/dt}{d\mathcal{L}_Q/dt}\,, \tag{12}$$

where $V_{\rm K\star} = \sqrt{GM_\star/R_\star}$ is the Keplerian velocity on the equator of the pulsar.

In Table 1, we summarize the mean length scales and their ratios produced by the KF model for the SMC-24 sample of 24 Magellanic pulsars (J. O'Leary et al. 2024a, 2025) in which canonical pulsar parameters ($M_\star = 1.4\,M_\odot$, $R_\star = 10$ km) were adopted.

The unusual scaling of Q by stellar values in the definition of $d\mathcal{L}_Q/dt$ in Equation (12) is one key reason for deriving simplified equations below. The actual angular momentum transfer rate from the inner edge of the disk, viz.,

$$\frac{d\mathcal{L}_d}{dt} \equiv Q\,R_m V_{\rm Km}\,, \tag{13}$$

is also introduced in part (5) below. In this definition, the product $R_m V_{\rm Km}$ is the specific angular momentum at radius R_m and $V_{\rm Km} = \sqrt{GM_\star/R_m}$.

(2) *Torques and stresses.* In X-ray outbursts ($\omega_s \ll 1$), the maximum torque on the pulsar is given by Equation (1) with $\omega_s \to 0$, viz.,

$$\frac{d\mathcal{L}_\star}{dt} = Q\sqrt{GM_\star R_m}\,, \tag{14}$$

which satisfies Equation (12) identically.

We note that in the propeller regime/marginal accretion limit (L. Stella et al. 1986; N. Andersson et al. 2005) $\omega_s \lesssim 1$, and the change in angular momentum $\mathcal{L}_\star$ is reduced by an additional factor of $(1 - \omega_s)$, as is seen in the KF torque Equation (1) (for more details, see part (8) below).

We can use the maximum torque balance of Equation (14) to obtain an expression for the $R\phi$ component of the stress tensor ($\mathcal{S}_{R\phi} = \rho_m V_m V_{\rm Km}$) at the inner edge of the accretion disk. Replacing Q by $4\pi\rho_m V_m R_m^2$ in Equation (14), we find that

$$\frac{d}{dt}\left(\frac{\mathcal{L}_\star}{\mathcal{V}_\star}\right) = 3\ell^6\mathcal{S}_{R\phi}\,, \tag{15}$$

where $\mathcal{V}_\star$ is the (constant) volume of the pulsar. Thus, $\mathcal{S}_{R\phi}$ is scaled by ℓ^6 to produce the (large) effective rate of change of the pulsar angular momentum density. But this torque is not used to estimate the stellar magnetic field $B_\star$ during X-ray outbursts of any type because it is valid only for $\omega_s = 0$. Instead, we take up the task of estimating $B_\star$ in the state $\omega_s \lesssim 1$ of minimal accretion in part (8) below.

(3) *KF β-frequencies.* Dividing β_2 by β_1 and simplifying the result by using Equations (2) and (3), we find that the ratio of these complicated quantities (Equations (6) and (7)) assumes an exceptionally simple form, viz.,

$$\frac{\beta_2}{\beta_1} = \omega_s\,. \tag{16}$$

This simple relation allows for an interpretation of the time-dependent HMXB models of J. O'Leary et al. (2024a, 2025) in the context of the magnetohydrodynamical simulations of stable/unstable accretion streams/hot spots carried out by M. M. Romanova & S. P. Owocki (2015) and A. A. Blinova et al. (2016): The measured β-frequencies show that the pulsars in the SMC-24 sample are segregated into two groups with fastness parameters of $\omega_s < 0.3$ and $\omega_s > 0.6$, respectively (see Figure 1 for details). The same grouping is also evident in the magnetospheres of the pulsars represented by the ratio ℓ^2 (Equation (11)), which is plotted in Figure 2, where the two

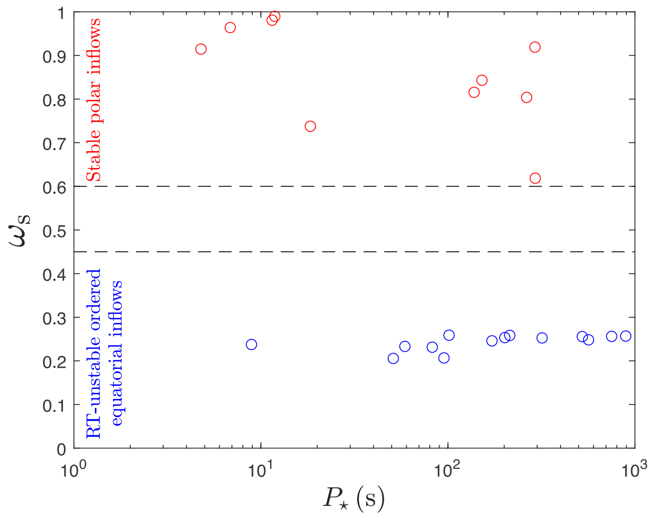

Figure 1. Ensemble-averaged fastness parameter ω_s vs. pulsar spin period $P_\star$ for the 24 HMXBs of the SMC-24 sample (J. O'Leary et al. 2025). Pulsars with $\omega_s > 0.6$ are expected to develop stable accretion streams channeled to the magnetic poles (e.g., A. A. Blinova et al. 2016). Pulsars with $\omega_s < 0.45$ are expected to develop two equatorial inflowing fingers by the action of RT instabilities. No objects have been found to persist in the intermediate regime of chaotic RT-unstable accretion, where several tongues penetrate the magnetosphere without merging and create hot spots all around the stellar surface.

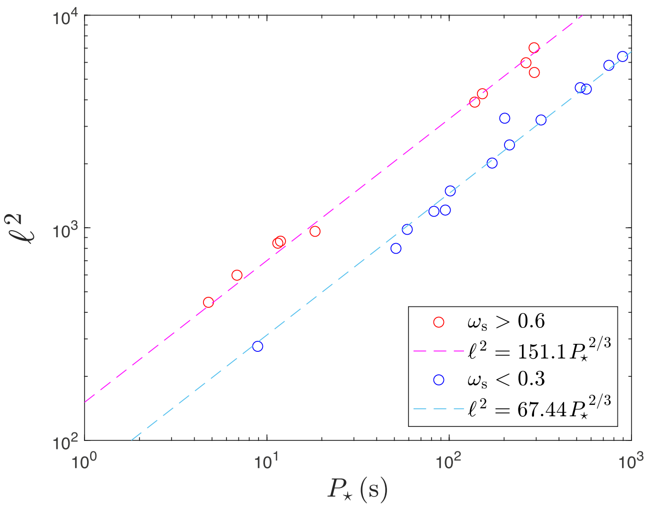

Figure 2. Normalized magnetospheric radius $\ell^2 = R_m/R_\star$ vs. pulsar spin period $P_\star$ for the 24 HMXBs of the SMC-24 sample (J. O'Leary et al. 2024a). As in Figure 1, the pulsars separate into two distinct groups. The dashed lines have a slope of 2/3 indicating that $R_m \propto P_\star^{2/3}$ but different magnetospheric sizes between the two groups (see also footnote 5).

sets of points both show that $R_m \propto P_\star^{2/3}$, with the intercepts differing by a factor of 2.24 owing to different mean ω_s values.[5]

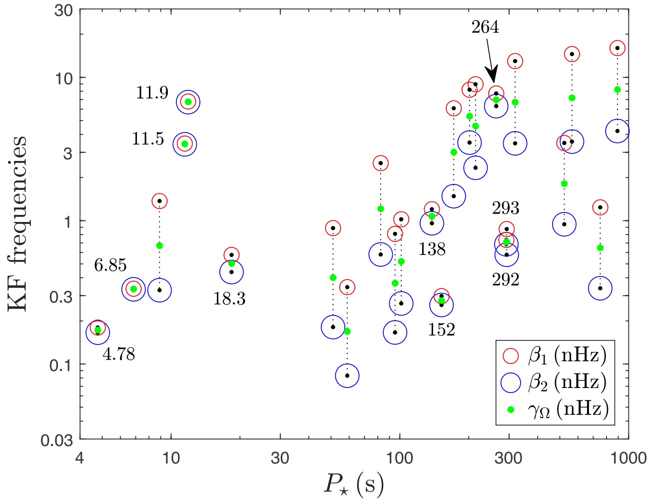

Figure 3. The two KF β-frequencies are plotted vs. pulsar spin period $P_\star$. Ten pulsars near spin equilibrium with $\beta_1 \approx \beta_2$ (and $\omega_s > 0.6$) are identified by their SXP names marked by asterisks in Table 1. Green filled circles represent γ_Ω values from Equation (17).

The product of the two KF β-frequencies produces another simple relation. Multiplying Equation (6) by Equation (7), substituting Equations (3)–(5), and simplifying the result, we obtain the geometric-mean relation

$$\gamma_\Omega = \sqrt{\beta_1 \beta_2}\,. \tag{17}$$

In spin-equilibrium KF models, these three KF frequencies coincide, and only γ_Ω is necessary in the so-called "linear KF models" (A. Melatos et al. 2023; J. O'Leary et al. 2024b). In the SMC-24 HMXB sample, 10 pulsars are found to be near spin equilibrium with $\beta_1 \approx \beta_2$; these pulsars are identified by their SXP names in Figure 3, in which the two β-frequencies and γ_Ω are plotted versus pulsar spin period $P_\star$.

(4) *Infall speed* $V_m(R_m)$ *and inner-edge density* $\rho_m(R_m)$. Dividing $S = \rho_m V_m^2/2$ by $Q = 4\pi\rho_m V_m R_m^2$, we obtain V_m from the ratio S/Q and the magnetospheric radius R_m, viz.,

$$V_m = 8\pi R_m^2 \left(\frac{S}{Q}\right). \tag{18}$$

Furthermore, the density ρ_m at the disk's inner edge can be expressed by the equation

$$4\pi\rho_m = \frac{Q}{R_m^2 V_m} = \frac{1}{\sqrt{2}}\left(\frac{\ell^{-3} Q}{R_\star j_{\mathrm{K}\star}}\right), \tag{19}$$

where $j_{\mathrm{K}\star} \equiv R_\star V_{\mathrm{K}\star}$ is the specific angular momentum at the stellar radius $R_\star$. The inflow speed $V_m(R_m)$ is commonly associated with the freefall speed $V_{\mathrm{ff}}(R_m) = \sqrt{2GM_\star/R_m}$, in which case

$$V_m = V_{\mathrm{ff}} = \sqrt{2}\, V_{\mathrm{Km}} = \sqrt{2}\, \ell^{-1} V_{\mathrm{K}\star}\,. \tag{20}$$

(5) *Inner-edge angular momentum transfer rate* $d\mathcal{L}_d/dt$. Since $V_{\mathrm{Km}} = \sqrt{GM_\star/R_m}$, the transfer rate (13) takes the equivalent forms

$$\frac{d\mathcal{L}_d}{dt} = \ell\left(\frac{d\mathcal{L}_Q}{dt}\right) = \frac{d\mathcal{L}_\star}{dt}\,. \tag{21}$$

These scalings are valid only for "extreme accretion" events (W. Kluźniak & J.-P. Lasota 2015; D. M. Christodoulou et al. 2018a), assumed to be 100% efficient (i.e., all the angular momentum inflowing from the disk's inner edge is added to the pulsar) without exhibiting delays due to hysteresis (e.g.,

---

[5] Equations (3)–(5) imply that $Q/S \propto \Omega_\star^{-5/3}$, and then Equation (2) gives $R_m \propto \Omega_\star^{-2/3} \propto P_\star^{2/3}$ in spin equilibrium. But the intercepts of the two lines plotted in Figure 2 depend on the average values of ω_s in the two groups: in fact, Equations (3) and (10) indicate that $R_m \propto \omega_s^{2/3} P_\star^{2/3}$.

A. Roy et al. 2022). On the other hand, in the propeller regime ($\omega_s \lesssim 1$), the KF transfer rates should be reduced by a factor of $(1 - \omega_s)$, as is also seen in Equation (1) for the stellar torque (see also Equation (33) below).

(6) *Alfvén speed* $V_{\rm A}(R_m)$. In general, the prominent ratio $Q/S \propto R_m^{5/2}$ (Equation (18) with $V_m \propto R_m^{-1/2}$) is effectively a measure of the magnetospheric radius R_m. For $\omega_s \lesssim 1$, this ratio reduces to

$$\frac{Q}{S} = 4\pi\sqrt{2}\left(\frac{R_c}{\Omega_\star}\right)\omega_s^{5/3}\,, \tag{22}$$

obtained from Equation (18) and the assumption in part (4) that $V_m = V_{\rm ff}$ at radius R_m. Then, we use $V_m = \sqrt{2}\ \omega_s^{-1/3} V_c$ (where $V_c = \Omega_\star R_c$), and the Alfvén speed squared at R_m, viz., $V_{\rm A}^{\,2}(R_m) \equiv B_m^2/(4\pi\rho_m) = B_m^2(R_m^2 V_m/Q)$ (by Equation (19)), takes the form

$$V_{\rm A}^{\,2} = \sqrt{2}\,(R_c j_c)\left(\frac{\omega_s}{Q}\right)B_m^2\,, \tag{23}$$

where the scaling factor $j_c \equiv R_c V_c$ is the specific angular momentum at the corotation radius, and, by Equations (18) and (22), the following identity holds near the propeller:

$$R_m V_m = \sqrt{2}\ j_c\ \omega_s^{1/3}\,, \tag{24}$$

which, by $R_m V_m = \sqrt{2}\,\ell j_{{\rm K}\star}$ and the nonmagnetic[6] equation $R_\star = \omega_s^{2/3}\ell^{-2}R_c$, is equivalent to the scaling relations

$$V_{{\rm K}\star} = \left(\frac{\ell}{\omega_s^{1/3}}\right)V_c \quad \text{and} \quad j_{{\rm K}\star} = \left(\frac{\omega_s^{1/3}}{\ell}\right)j_c\,. \tag{25}$$

We note that by multiplying these two equations, we obtain the identity $V_c j_c = V_{{\rm K}\star} j_{{\rm K}\star}$, which is a restatement of the definition that $\Omega_\star \equiv \sqrt{GM_\star/R_c^3}$ at the corotation radius.

The factor (ω_s/Q) in Equation (23) encompasses both limiting cases of accretion from the viewpoint of the magnetosphere: (i) For marginal accretion in the propeller regime ($\omega_s \lesssim 1$, $R_m \lesssim R_c$), $V_{\rm A}$ is large and the mass inflow rate $Q \propto 1/V_{\rm A}^{\,2}$ is small. (ii) For extreme accretion ($\omega_s \ll 1$), the magnetosphere is fully compressed by the disk ($R_m \ll R_c$), and $V_{\rm A}$ and $1/Q$ are small as well.

(7) *Stellar magnetic field* $B_\star$. The magnetic field $B_m(R_m)$ (Equation (23)) at the disk–magnetosphere boundary obeys the scaling relation

$$B_\star = B_m\left(\frac{R_m}{R_\star}\right)^3 = B_m\ell^6\,, \tag{26}$$

where $B_\star$ is the magnetic field on the surface of the pulsar. The ℓ^6 scaling is striking, just as in Equation (15) as well.

(a) Disk $\mathcal{S}_{R\phi}$: Eliminating ℓ^6 between Equations (15) and (26) and B_m in favor of R_m^3, we find that

$$R_m^3\,\mathcal{S}_{R\phi} = \frac{1}{4\pi}\left(\frac{d\mathcal{L}_\star}{dt}\right). \tag{27}$$

The two factors on the left-hand side compete against one another; they vary in opposite directions, although $\mathcal{S}_{R\phi}$ wins in both limiting cases: (i) during marginal accretion, R_m has expanded out toward corotation, whereas $\mathcal{S}_{R\phi}$ has decreased dramatically, resulting in only minimal pulsar spin changes; and (ii) during X-ray outbursts, R_m is compressed severely, but $\mathcal{S}_{R\phi}$ overloads the magnetic field lines with inflowing matter, thus producing very strong torques and rapid spin changes.

The influence of the disk's $\mathcal{S}_{R\phi}$ on the pulsar's spin rate of change is perhaps better characterized by introducing B_m in Equation (27): since $B_m \propto R_m^{-3}$, then $\mathcal{S}_{R\phi} \propto B_m(d\mathcal{L}_\star/dt)$, where B_m varies in the opposite direction, albeit much more slowly so as to not invert the direct proportionality of $\mathcal{S}_{R\phi} \propto (d\mathcal{L}_\star/dt)$.

(b) Pulsar $B_\star$: The strength of the surface magnetic field $B_\star$ is commonly estimated in the propeller regime (where $\omega_s \lesssim 1$, $R_m \lesssim R_c$) by various complicated equations involving several stellar and disk quantities. Here, as in the treatments of N. Andersson et al. (2005) and A. Papitto & D. F. Torres (2015), we use the equatorial dipolar value of $B_\star$ (i.e., no $1/2$ factor corresponding to a single "magnetic pole"; G. B. Rybicki & A. P. Lightman 2004, p. 324), which is consistent with the equatorial value of B_m at radius R_m in Equation (26), viz., $B_\star = \mu_\star R_\star^{-3}$, and we find from Equation (8) that

$$B_\star^2 = \left(\frac{V_{{\rm K}\star}\,Q}{\sqrt{8}\ R_\star^2}\right)^{12/5}(2\pi\ S)^{-7/5}\,, \tag{28}$$

where the mean values of Q and S are returned by the unscented KF. However, the measured mass inflow rate Q is generally expected to be substantially higher than the actual propeller value Q_p (see part (8) below). Thus, we expect that $B_\star$ may be overestimated by the KF for a large number of pulsars (as shown in Section 3.1 below) that do not spend most of their time in quiescence. We revisit this issue in Section 3.2 below.

Alternatively, an estimate of $B_\star$ can be obtained in terms of the long-term spin period rate of change $dP_\star/dt \equiv \dot{P}_\star$ (the so-called "P-dot") measured by J. Yang et al. (2017) for all SMC pulsars over a period of ~20 yr. The alternative equation for $B_\star^2$ takes an especially simple form (no rational powers on the variables and no dependence on the adopted definition of $\mu_\star$), viz.,

$$B_\star^2 = \frac{\sqrt{2}}{5\pi}\left(\frac{GM_\star^2}{R_\star^4}\right)|\dot{P}_\star|\,, \tag{29}$$

where we have used the moment of inertia $I_\star = 2M_\star R_\star^2/5$ in intermediate steps. The factor in parentheses has dimensions of [energy density] or [pressure] (which is consistent with the dimensions of $B_\star^2$), whereas the long-term P-dot ($\dot{P}_\star$) is a dimensionless quantity.

(c) Physical Interpretation: Notably, $GM_\star^2/R_\star^4 = 4\pi g_\star\Sigma_\star$ in Equation (29), where $g_\star = GM_\star/R_\star^2$ is the surface gravity and $\Sigma_\star \equiv M_\star/(4\pi R_\star^2)$ is the surface density of the pulsar, thus indicating the nature of the stellar properties that couple to the long-term value of P-dot to yield the surface dipolar magnetic field; in particular,

$$B_\star\ =\ 1.06\sqrt{(g_\star\Sigma_\star)|\dot{P}_\star|}\ . \tag{30}$$

The parentheses under the square root have meaning. As in many equations of physics (e.g., Equations (17) and (11) written as $\ell = \sqrt{R_m/R_\star}$), the square root represents the geometric mean of two factors (D. M. Christodoulou & D. Kazanas 2023), and it is such a geometric mean that

---

[6] Equations (10) and (11) combine to produce the nonmagnetic length ratio $R_c/R_\star = (\ell/\omega_s^{1/3})^2$.

effectively determines $B_\star$ in the P-dot case as well. The parentheses highlight the factor that describes the intrinsic pulsar properties, whereas the other factor of the geometric mean (the P-dot) describes an external influence due to the accretion of matter.

(8) *Propeller mass inflow rate Q_p and KF frequency γ_Ω in spin equilibrium*. Consistency between Equations (29) and (9) (with $(\mu_\star)_{\rm se}{=}R_\star^3(B_\star)_{\rm se}$, $\Omega_\star^2{=}GM_\star/R_c^3$, and $P_\star = 2\pi/\Omega_\star$) near spin equilibrium yields a relation between the propeller inflow rate Q_p and the corresponding long-term P-dot value $\dot{P}_\star$. Combining these equations, letting $Q \rightarrow Q_p$, and solving for Q_p, we find that

$$Q_p = \frac{4I_\star|\dot{P}_\star|}{R_c^2 P_\star}\,. \tag{31}$$

In general, we expect that the propeller $Q_p \ll Q$ measured by the KF (unless the X-ray luminosity of a source undergoes minimal fluctuations during its entire history), in which case we expect that $Q_p \approx Q(1 - \omega_s)$ in the propeller regime, or, by Equation (4), that the absolute value of the long-term P-dot is

$$|\dot{P}_\star| \approx \frac{1}{4} P_\star\,(1 - \omega_{\rm s})\,\gamma_\Omega\,, \tag{32}$$

where the mean values for the right-hand side are produced by the unscented KF (J. O'Leary et al. 2024a, 2025).

In Equation (32), the torque frequency $\gamma_\Omega{=}\sqrt{\beta_1\beta_2}$ is scaled down by $(1 - \omega_s)$ to produce the effective P-dot value in the propeller regime. The same scaling also appearing in the stellar torque Equation (1) should be applied to the spin-equilibrium Equations (4) and (5) as well, viz.,

$$\begin{bmatrix} Q_p \\ S_p \end{bmatrix} = (1 - \omega_s)\,\gamma_\Omega \begin{bmatrix} Q \\ S \end{bmatrix}, \tag{33}$$

in the propeller regime. In this case, the factor $Q^{12/5}S^{-7/5}$ in Equation (28) shows that the surface dipolar magnetic field $B_\star$ produced by the unscented KF must be scaled accordingly to its propeller value $(B_\star)_p$, viz.,

$$(B_\star)_p = \sqrt{1 - \omega_s}\,B_\star\,. \tag{34}$$

This scaling of the KF values is consequential in obtaining agreement for $B_\star$ between the two methods (long-term P-dot and KF), as delineated in Section 3.2 below.

3. Discussion and Conclusion

3.1. Comparison of Pulsar Magnetic Fields

In Figure 4, we compare the $B_\star$ values measured by the KF (Equation (28); J. O'Leary et al. 2024a) to the corresponding $B_\star$ values determined from Equation (29) for the 24 pulsars in the SMC-24 sample. In the latter part of our calculations, we have used the P-dot values determined in the most recent SMC HMXB pulsar survey (J. Yang 2017; J. Yang et al. 2017). The canonical pulsar parameters of $M_\star$ and $R_\star$ are used throughout.

The quantum limit of $B_{\rm QL} = 44.14$ TG (I. Wasserman & S. L. Shapiro 1983) is also shown by a horizontal dotted line. Both sets of points show that the rise of $B_\star$ values is interrupted near the quantum limit, although a few points seem to lie above $B_{\rm QL}$. The largest KF deviation occurs for SXP 264 ($B_\star = 2.5B_{\rm QL}$), although the expectation from P-dot (red point) was that $B_\star = 0.2B_{\rm QL}$, i.e., 12 × lower. Typically, 11 of 24 objects show relative $B_\star$ ratios of 0.5–2, whereas another 11 objects show larger deviations with ratios of 2.4–6.7. SXP 11.5 and SXP 11.9 are the clear outliers with $B_\star$ ratios > 6. They are the cause of the big "blue bump" seen in the Kalman three-point moving average across $P_\star$ values of 7-42 s.

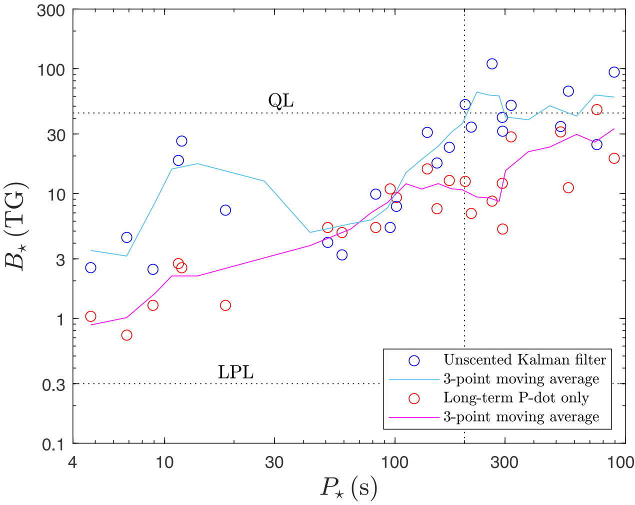

Figure 4. Surface magnetic field $B_\star$ vs. spin period $P_\star$ for the 24 SMC pulsars in our sample (Equations (28) and (29) in blue and red, respectively). The scales are base-10 logarithmic. The quantum limit $B_{\rm QL} = 44.14$ TG and the lowest propeller line (LPL) $B_{\rm LPL} = 0.3$ TG are shown by horizontal dotted lines. The solid lines represent the three-point moving average across $P_\star$ values in each data set (extrapolated to the edges). The KF blue points appear to roughly level out beyond $P_\star \sim 200$ s, the boundary marked by the vertical dotted line—although some overshoots to much higher $B_\star$ values than $B_{\rm QL}$ are seen at three $P_\star$ values.

In very long period pulsars (say, $P_\star > 200$ s), it seems as though both sets of points may be leveling out, albeit at differing $B_\star$ values (at ∼28 and ∼44 TG, respectively). However, some randomly distributed overshoots obscure this trend, just as they obscure the mild rise of the blue points for $P_\star < 20$ s. These overshoots cannot probably be waived aside on statistical grounds, as the $B_\star$ values are seen to increase by one order of magnitude. On the other hand, the rising trend of $B_\star$ is evident in the intervals of $P_\star = 50$–200 s (blue points) and 10–130 s (red points), respectively. These trends are highlighted best by the moving averages shown by solid lines in Figure 4.

A flattening trend of $B_\star$ at very long spin periods has not been seen in past studies of SMC HMXBs. If confirmed by future studies, it will help establish the KF analysis as a powerful tool for the studies of X-ray binary pulsars. In their "high" magnetic field case, H. Klus et al. (2014) determined $B_\star(P_\star)$ values that increased linearly far beyond the quantum limit, and the study of C. R. D'Angelo (2017) produced a scaled-down version of the same results that barely reached up to $\sim B_{\rm QL}$, but this study preserved the original linear rising trend first seen in the results of H. Klus et al. (2014) and H. Klus (2015).

In our previous KF investigation, we have compared the unscented KF output to the original results of H. Klus et al. (2014) in Figure 5 of J. O'Leary et al. (2024a), where KF magnetic moments are seen to level out at about $\mu_\star = \mu_{\rm QL}$ beyond spin periods of $P_\star \sim 200$ s, whereas the older "high" solution proceeds linearly up to $\sim 10^3$ TG at spin periods of $P_\star \gtrsim 10^3$ s. This conspicuous discrepancy was also explained in the same figure: the calculations of H. Klus et al. (2014)

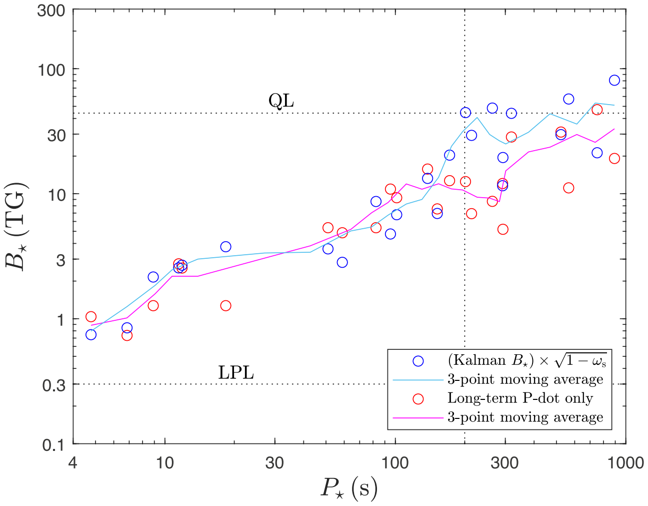

Figure 5. Same as Figure 4, but the magnetic field values produced by the KF were scaled down to the propeller regime by a factor of $\sqrt{1-\omega_s}$ (blue points), matching the propeller values (red points) obtained from the (20 yr) long-term measurements of P-dot values (J. Yang et al. 2017). This scaling (Equations (34) and (28)) results in very good agreement between the two $B_\star$ determinations out to $P_\star \sim 200$ s (vertical dotted line), yet a discrepancy of up to 4× remains for longer-period pulsars with $P_\star \sim 200$–300 s. Beyond $P_\star \sim 300$ s, both moving averages (colored solid lines) come up against the quantum limit of $B_{\rm QL} = 44.14$ TG.

showed mass inflow rates of $Q \gtrsim 8 \times 10^{-10}\ M_\odot\ {\rm yr}^{-1}$ for all SMC sources, whereas the KF produced Q values smaller by 1–2 orders of magnitude for the longer-period SMC sources with $P_\star > 200$ s.

3.2. Scaling KF Output to the Propeller Regime

For spin periods longer than $P_\star \sim 100$ s, the known set of propeller lines in the Magellanic HMXB pulsars dip down to currently unobservable X-ray luminosities of $L_X \leqslant 10^{32}$ erg s^{-1} (D. M. Christodoulou et al. 2017). For such pulsar spin periods, the observed X-ray luminosities do certainly describe higher excited accretion states, irrespective of the observed flux variations (H. Klus et al. 2014; H. Klus 2015; D. M. Christodoulou et al. 2016; C. R. D'Angelo 2017). For shorter spin periods, the low-L_X propeller states of many SMC HMXB pulsars have already been observed (J. Yang et al. 2017, and references therein), although the observations are not numerous in the data series spanning about 20 yr.

Most of the SMC HMXB X-ray observations to date have detected pulsars in their excited states in which the measured mean Q values are higher than the Q_p propeller values that characterize states of minimal accretion (see the review of X-ray observations by D. M. Christodoulou et al. 2016).

Seeking a description of marginal accretion near propeller lines, C. R. D'Angelo (2017) devised a method to scale down the SMC RXTE results of H. Klus et al. (2014), concluding that the $B_\star$ values of Magellanic HMXB pulsars do not have to exceed magnetar strengths. Although generally successful in this respect, this type of scaling is rather arbitrary and not easily justifiable. We have also sought to scale down the KF $B_\star$ values shown in Figure 4 by reducing the mean values of the mass inflow rate Q and the Maxwell stress S by a factor of $(1-\omega_s)$ (Equation (33)). The $B_\star$ points shown in blue color in Figure 4 are then effectively reduced by $\sqrt{1-\omega_s}$, and the results thus obtained for "marginal accretion" are depicted in Figure 5, again in blue/cyan colors.

Table 2
Typical Relative Errors $|\Delta B_\star|/B_\star$ Propagated in the KF Method, the P-dot Method, and the Averaged $B_\star$ Values between the Two Methods

Error Placement	Kalman (SXP)	P-dot (SXP)	Averaged (SXP)
Minimum	0.033 (565)	0.093 (323)	0.114 (323)
Median	0.155 (293)	0.571 (11.5)	0.791 (82.4)
Mean	0.731	0.711	1.236
Maximum	6.018 (6.85)	2.464 (264)	6.101 (6.85)
SXP 11.9[a]	13.443	0.167	13.444
SXP 756[b]	0.041	0.195	0.199

Notes.

[a] SXP 11.9, a clear outlier because of its large value of $\omega_s = 0.990$, is listed separately at the bottom of the table.

[b] SXP 756 with $|\Delta B_\star| = 10.6$ TG shows the largest averaged value above the quantum limit ($B_\star = 53.1$ TG), although $B_{\rm QL}$ falls within the error bar. The same observation holds for SXP 893 with a much larger error bar of $|\Delta B_\star| = 45.1$ TG and the most extreme KF value above $B_{\rm QL}$ ($B_\star = 80.9$ TG).

In Figure 5, the agreement with the long-term P-dot $B_\star$ values (red points, same as those in Figure 4) is very good, which could be surprising. Although we see a few overshoots that reach the quantum limit, the three-point moving averages appear to flatten out at ∼30–40 TG for $P_\star > 300$ s.

Furthermore, the large discrepancies at short spin periods ($P_\star < 20$ s) have all but disappeared. A discrepancy of up to 4× in $B_\star$ that remains in Figure 5 is confined right around pulsar spin periods of $P_\star \sim 200$–300 s. We have traced this factor of 4 to the effective values of P-dot obtained from the KF output data (Equation (32)). We attribute this mismatch to the small number of observations (∼10) that were used to determine the 20 yr long-term P-dot values (J. Yang 2017) of the five SMC X-ray sources listed in rows 15–19 of Table 1; thus, we believe that the blue KF points shown in Figure 5 and their three-point moving average (cyan solid line) should give a more accurate representation of the pulsar magnetic fields in our SMC-24 HMXB sample.

Table 2 summarizes typical relative errors propagated in both determinations of the $B_\star$ values. The error bars in the KF method were calculated from the 1σ errors in Q, S, and ω_s reported by the KF data analysis of J. O'Leary et al. (2024a). The error bars in the P-dot method were calculated from the $\dot{P}_\star$ 1σ errors reported by J. Yang et al. (2017). The relative errors of the averaged $B_\star$ values are listed in the last column; they are applicable to the points plotted in Figure 6.

3.3. Conclusion

In Figure 6, we plot the mean values of two sets of three-point moving averages shown in Figure 5. These values represent our best estimates of surface magnetic fields $B_\star$ over pulsar spin periods of up to $P_\star = 800$ s, where $B_\star = B_{\rm QL}$. The best-fit curve of the mean $B_\star$ values, viz.,

$$B_\star = \left(\frac{P_\star}{5.150\ {\rm s}}\right)^{0.750}\ {\rm TG}\,, \tag{35}$$

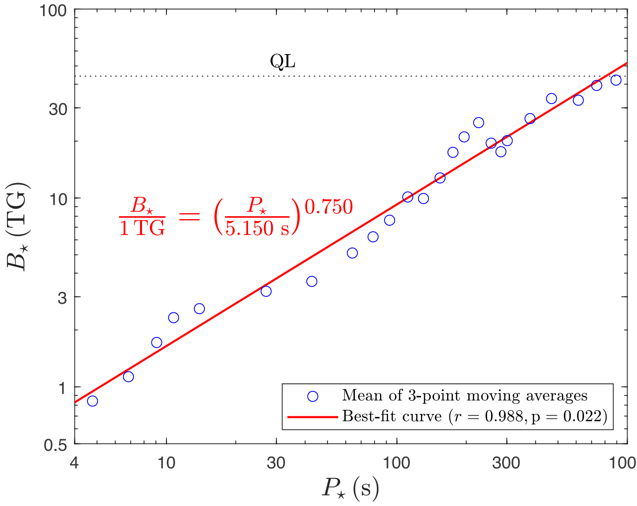

Figure 6. The mean $B_\star$ values of the three-point moving averages from Figure 5 are fitted by least squares. The best-fit curve is shown in red color.

is also plotted in Figure 6 as a red line; in the log-log scales of the figure, it takes the linear form

$$\log\left(\frac{B_\star}{1\ \mathrm{TG}}\right) = C_0 + C_1 \cdot \log\left(\frac{P_\star}{1\ \mathrm{s}}\right), \tag{36}$$

where $C_0 = -0.534 \pm 0.052$ and $C_1 = 0.750 \pm 0.025$. The quality of the least-squares fit is acceptable as evidenced by the correlation coefficient $r = 0.988$ and a p-value of 0.022, better than the 95% confidence level.

The slope of $C_1 = 0.750$ in Equation (36) is lower than the corresponding values derived from the models of H. Klus et al. (2014) and C. R. D'Angelo (2017). Least-squares fitting of their published data indicates that the slopes are $C_1 \approx 1.0$ in both data sets. One reason for such higher slopes is that, unlike our results (Section 3.2), the previously determined $B_\star$ values show no flattening trend at long spin periods (Section 3.1). Thus, it becomes an important issue for future studies of HMXB pulsars to determine an accurate slope of the $\log B_\star(\log P_\star)$ relation, hopefully using larger data sets than our SMC-24 sample and more HMXB sources with $P_\star < 200$ s (for the reasons described below).

Equation (35) is certainly not universal, as a preliminary comparison with previous magnetic field estimates indicates:

(a) In millisecond binary pulsars (e.g., Aquila X-1, SAX J1808.4−3658; D. M. Christodoulou et al. 2018b), the $B_\star$ values differ by factors of $\gtrsim 30$.

(b) In Galactic HMXBs and Be transients with cyclotron resonance absorption features and $P_\star > 200$ s (e.g., 1A 1118−616, Vela X-1, 4U 1907+09; R. Staubert et al. 2019), the $B_\star$ values differ by factors of 6–14. Such large offsets are understandable: the best-fit line in Figure 6 continues to rise monotonically throughout, whereas Figure 5 shows that the (blue) KF $B_\star$ values level out to $B_{\mathrm{QL}} = 44.14$ TG for $P_\star > 200$ s. More importantly, it is not expected that Equation (35) will be valid for wind-fed supergiant (Sg) HMXBs such as Vela X-1 and 4U 1907+09.

(c) In the same sample limited to pulsars with $P_\star < 200$ s, quite a few pulsars have $B_\star$ values to within a factor of 2 relative to the cyclotron-determined values of B_{cyc} (4U 0115+63, Swift 1626.6−5156, NGC300 ULX 1, Cep X-4, 1A 0535+262), whereas a few other pulsars have $B_\star$ values to within a factor of ∼4 (V0332+53, EXO 2030+375, Sg IGR 17544−2619).

(d) Equation (35) seems to fare better in the cases of the pulsars M82 X-2 (D. M. Christodoulou et al. 2018b, and references therein) and SMC X-2 (A. Roy et al. 2022, and references therein), two pulsars that have been observed and studied exhaustively in the past. The dipolar magnetic field values previously obtained in the propeller regime are $B_p = 0.41$ TG (M82 X-2) and $B_p = 1.2$ TG (SMC X-2), and we have determined from Equation (35) that $B_\star \simeq 0.9 B_p$ and $B_\star \simeq 0.5 B_p$, respectively.

In conclusion, Equation (35) appears to be applicable for Be HMXB and Be transient X-ray sources with $P_\star < 200$ s, but deviations of $B_\star$ from the actual magnetic field values by factors of 2–4 should be anticipated in future Be HMXB pulsar studies.

Acknowledgments

We thank the reviewer of the paper for comments and suggestions that helped us improve the presentation. This research project was facilitated in part by the following funding agencies and programs: NSF-AAG, grant 2109004; NASA Astrophysics Data Analysis Program (ADAP), grants NNX14AF77G and 80NSSC18K0430; Lowell Center for Space Science and Technology (LoCSST) of the University of Massachusetts Lowell; and Australian Research Council Centre of Excellence for Gravitational Wave Discovery, grant CE170100004.

ORCID iDs

Dimitris M. Christodoulou https://orcid.org/0000-0002-7652-2206
Joseph O'Leary https://orcid.org/0000-0002-6547-2039
Andrew Melatos https://orcid.org/0000-0003-4642-141X
Tom Kimpson https://orcid.org/0000-0002-6542-6032
Sayantan Bhattacharya https://orcid.org/0000-0001-8572-8241
Nicholas J. O'Neill https://orcid.org/0009-0007-3868-5227
Silas G. T. Laycock https://orcid.org/0000-0002-8427-0766
Demosthenes Kazanas https://orcid.org/0000-0002-7435-7809

References

Andersson, N., Glampedakis, K., Haskell, B., & Watts, A. L. 2005, MNRAS, 361, 1153

Antoniou, V., Zezas, A., Hatzidimitriou, D., & Kalogera, V. 2010, ApJL, 716, L140

Becker, P. A., Klochkov, D., Schönherr, G., et al. 2012, A&A, 544, A123

Blinova, A. A., Romanova, M. M., & Lovelace, R. V. E. 2016, MNRAS, 459, 2354

Christodoulou, D. M., & Kazanas, D. 2023, Ast, 2, 235

Christodoulou, D. M., Laycock, S. G. T., & Kazanas, D. 2018a, MNRAS, 478, 3506

Christodoulou, D. M., Laycock, S. G. T., & Kazanas, D. 2019, RAA, 19, 146

Christodoulou, D. M., Laycock, S. G. T., Kazanas, D., & Contopoulos, I. 2018b, RAA, 18, 142

Christodoulou, D. M., Laycock, S. G. T., Yang, J., & Fingerman, S. 2016, ApJ, 829, 30

Christodoulou, D. M., Laycock, S. G. T., Yang, J., & Fingerman, S. 2017, RAA, 17, 59

Coe, M., Bartlett, E., Bird, A., et al. 2015, MNRAS, 447, 2387
D'Angelo, C. R. 2017, MNRAS, 470, 3316
D'Angelo, C. R., & Spruit, H. C. 2010, MNRAS, 406, 1208
D'Angelo, C. R., & Spruit, H. C. 2012, MNRAS, 420, 416
Frank, J., King, A., & Raine, D. 2002, Accretion Power in Astrophysics (Cambridge: Cambridge Univ. Press)
Galache, J., Corbet, R., Coe, M., et al. 2008, ApJS, 177, 189
Gardiner, L. T., & Noguchi, M. 1996, MNRAS, 278, 191
Garmire, G. P., Bautz, M. W., Ford, P. G., Nousek, J. A., & Ricker, G. R., Jr. 2003, Proc. SPIE, 4851, 28
Ghosh, P., & Lamb, F. 1979, ApJ, 234, 296
Haberl, F., Maitra, C., Vasilopoulos, G., et al. 2022, A&A, 662, A22
Haberl, F., & Sturm, R. 2016, A&A, 586, A81
Ho, W. C. G., Klus, H., Coe, M. J., & Andersson, N. 2014, MNRAS, 437, 3664
Jackson, J. D. 1962, Classical Electrodynamics (New York: Wiley), 193
Jahoda, K., Markwardt, C. B., Radeva, Y., et al. 2006, ApJS, 163, 401
Jaisawal, G. K., & Naik, S. 2016, MNRAS, 461, L97
Klus, H. 2015, PhD Thesis, Univ. Southampton
Klus, H., Ho, W. C. G., Coe, M. J., et al. 2014, MNRAS, 437, 3863
Kluźniak, W., & Lasota, J.-P. 2015, MNRAS, 448, L43
Maitra, C., Paul, B., Haberl, F., & Vasilopoulos, G. 2018, MNRAS, 480, L136
Melatos, A., O'Neill, N. J., Meyers, P. M., & O'Leary, J. 2023, ApJ, 944, 64
Menou, K., Esin, A. A., Narayan, R., et al. 1999, ApJ, 520, 276
Mukherjee, D., Bult, P., van der Klis, M., & Bhattacharya, D. 2015, MNRAS, 452, 3994
Mushtukov, A. A., Suleimanov, V. F., Tsygankov, S. S., & Poutanen, J. 2015, MNRAS, 447, 1847
Mushtukov, A. A., Suleimanov, V. F., Tsygankov, S. S., & Zwart, S. P. 2021, MNRAS, 503, 5193
Nishimura, O. 2013, PASJ, 65, 84
Nishimura, O. 2014, ApJ, 781, 30
Nishimura, O. 2015, ApJ, 807, 164
O'Leary, J., Melatos, A., Kimpson, T., et al. 2024a, ApJ, 971, 126
O'Leary, J., Melatos, A., Kimpson, T., et al. 2025, ApJ, 981, 150
O'Leary, J., Melatos, A., O'Neill, N. J., et al. 2024b, ApJ, 965, 102
Papitto, A., & Torres, D. F. 2015, ApJ, 807, 33
Romanova, M. M., & Owocki, S. P. 2015, SSRv, 191, 339
Roy, A., Cappallo, R., Laycock, S. G. T., et al. 2022, ApJ, 936, 90
Rybicki, G. B., & Lightman, A. P. 2004, Radiative Processes in Astrophysics (Weinheim: Wiley-VCH), 324
Staubert, R., Trümper, J., Kendziorra, E., Klochkov, D., et al. 2019, A&A, 622, A61
Stella, L., White, N. E., & Rosner, R. 1986, ApJ, 308, 669
Stierhof, J. J. R., Sokolova-Lapa, E., Berger, K., et al. 2025, A&A, 698, A308
Strüder, L., Briel, U., Dennerl, K., et al. 2001, A&A, 365, L18
Townsend, L., Coe, M., Corbet, R., & Hill, A. 2011, MNRAS, 416, 1556
Wang, Y.-M. 1995, ApJL, 449, L153
Wasserman, I., & Shapiro, S. L. 1983, ApJ, 265, 1036
Yang, J. 2017, PhD Thesis, Univ. Massachusetts Lowell
Yang, J., Laycock, S. G. T., Christodoulou, D. M., et al. 2017, ApJ, 839, 119